ASME Journal of Energy Resources Technology
Online journal at:
https://asmedigitalcollection.asme.org/energyresources

Multi-Objective Optimization of a Bi-Metal High-Temperature Recuperator for Application in Concentrating Solar Power

Jacob A. Bryan[1]
Department of Mechanical and Aerospace Engineering,
Utah State University,
4130 Old Main Hill,
Logan, UT 84322
e-mail: jacob.bryan@usu.edu

Aiden S. Meek
Department of Mechanical and Aerospace Engineering,
Utah State University,
4130 Old Main Hill,
Logan, UT 84322
e-mail: aiden.meek@usu.edu

Hailei Wang
Department of Mechanical and Aerospace Engineering,
Utah State University,
4130 Old Main Hill,
Logan, UT 84322
e-mail: hailei.wang@usu.edu

Supercritical CO_2 closed Brayton cycles are a major candidate for future power cycle designs in concentrating solar power applications, with high-temperature recuperators playing an essential role in realizing their high thermal efficiency. Printed circuit heat exchangers (PCHEs) are often chosen for this role due to their thermal-hydraulic and mechanical performance at high temperatures and pressures, all while remaining compact. However, PCHEs can be costly because of the high-performance materials demanded in these applications, and the heat exchanger internal geometry is restricted by their manufacturing process. Additively manufactured heat exchangers can address both of these shortcomings. This work proposes a modular bi-metal high-temperature recuperator with integrated headers to be produced with additive manufacturing. Beginning with existing PCHE channel geometries, a 1D heat exchanger model is developed. Then, multi-objective optimization is used to maximize the heat transfer effectiveness of a lab-scale device while limiting its size. Two distinct channel geometries emerge from the optimization. Optimal designs achieve up to 88% effectiveness with negligible pressure drop. Deterioration of effectiveness due to axial conduction of heat in the heat exchanger walls is found to be a notable problem for lab-scale PCHEs, and the optimal designs obtained here minimize its detrimental effects. A sensitivity analysis reveals that the effectiveness of the recuperator is much less sensitive to variation in mass flowrate in off-design operation when axial conduction is significant, while increasing the length of the device easily increases effectiveness. [DOI: 10.1115/1.4062522]

Keywords: multi-objective optimization, sensitivity analysis, additive manufacturing, recuperator, concentrating solar power

1 Introduction

This paper presents the design of a high-temperature recuperator (HTR) for a supercritical CO_2 (sCO_2) Brayton cycle. The paper includes the results of analysis as well as the methods used to perform the analysis.

Many recent designs for concentrating solar power and other high-temperature power cycle applications use the sCO_2 Brayton cycle to operate at a high efficiency [1,2]. SCO_2 Brayton cycles have been shown to have greater thermal efficiency than steam Rankine cycles for maximum cycle temperatures exceeding 500 °C, with regenerative and recompression cycle designs having the highest efficiency [3]. An example of such a cycle is illustrated in Fig. 1. Recuperators are used to recover residual heat in the working fluid after expansion in the turbine, and a recuperator with high effectiveness is required to gain the maximum efficiency increase [4].

Another advantage of using the sCO_2 Brayton cycle is size reduction of heat exchangers and turbomachinery. Typically, shell and tube heat exchangers (STHEs) are very large; some compact heat exchanger designs can reduce this size by 85% or better. Printed circuit heat exchangers (PCHEs) are one common type of compact heat exchangers. PCHEs can have heat transfer surface area densities exceeding 700 m^2/m^3, whereas STHEs generally have surface area densities around 100 m^2/m^3 [5]. Figure 2 illustrates this size reduction. The increase in efficiency and reduction in capital, operational, and maintenance expenses due to smaller machinery in sCO_2 Brayton cycles combines to reduce levelized cost of electricity by as much as 10–20% [6].

Significant work is underway to characterize the heat transfer performance of sCO_2 in novel heat exchanger designs, both experimentally and numerically [7–10]. SCO_2 heat exchanger designs have been the focus of many design optimization studies (see Refs. [11,12] and the references therein). Sometimes the resulting designs would be difficult to manufacture using traditional methods and would be best suited by additive manufacturing (AM) techniques [13]. In the broader heat exchanger optimization

[1]Corresponding author.

Contributed by the Advanced Energy Systems Division of ASME for publication in the Journal of Energy Resources Technology. Manuscript received December 5, 2022; final manuscript received April 21, 2023; published online June 20, 2023. Assoc. Editor: Heejin Cho.

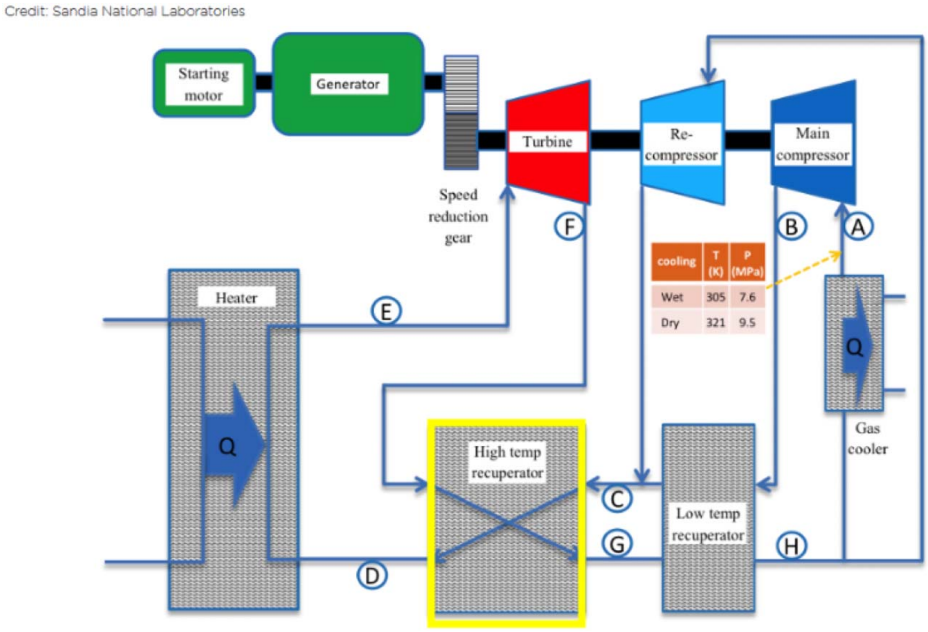

Fig. 1 A regenerative Brayton cycle design with a higher temperature recuperator (highlighted) [4]

literature, non-traditional designs have shown potential for both increased heat transfer performance and reduced pressure drop [14,15].

The HTR of a sCO_2 Brayton cycle operates at temperatures between 200 °C and 500 °C and pressures of up to 20–30 MPa. PCHEs are well suited for these design conditions, but these temperatures and pressures demand high-performance materials such as expensive nickel superalloys. The total cost of a PCHE depends significantly on both the thermal-hydraulic performance of the device and its manufacturing cost, including material costs, so careful consideration of both aspects are essential for cost-effective operation [16]. One potential solution to this expensive material problem is to use these high-performance materials only where their performance is truly needed, minimizing material costs without sacrificing thermal-hydraulic performance.

Material costs for the HTR can be minimized using these high-performance materials only where their strength is necessary. Lower performance metals like stainless steel 316L are sufficiently strong for these pressures at the lower temperatures in this operating condition range, and higher performance materials are needed only as the temperature increases beyond a certain point. Rather than divide the HTR into two devices, with the cost and complexity that would entail, a modular bimetallic heat exchanger could tailor its material to the operating conditions in each portion of the device while still being a single metallic body. Figure 3 shows the modular plan for the heat exchanger, having high-temperature compatible materials at one end, and cheaper lower temperature compatible materials at the other. This novel concept is the focus of this work.

Additive manufacturing makes the manufacturing of such bi-metal designs possible. Metal additive manufacturing has been around for several years and has shown capability in printing heat exchangers, blending alloys, and bimetallic bodies. There are several methods for additive manufacturing of metal parts, two of which, powder bed fusion and directed energy deposition (DED), are used in the design.

Powder bed fusion uses layers of metal powder fuzed together using lasers or electron beams. The process chosen for this project melts the metal powder under the laser causing the powder to bond to the solid material beneath it creating one solid part. The part is printed layer by layer, lasers melting the appropriate

Fig. 2 Size comparison between a shell and tube heat exchanger and a printed circuit heat exchanger with comparable heat transfer area [5]

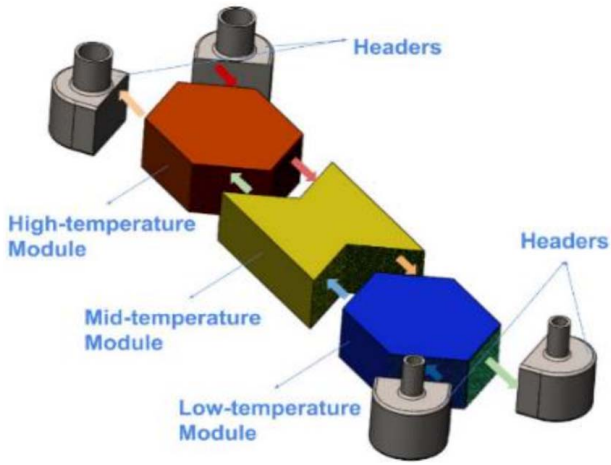

Fig. 3 Conceptual design of a bi-metal modular recuperator with integrated headers

locations to print the part as a whole. However, this process is unable to mix alloys and cannot change alloys partway through the printing process. Nor can this printer start printing on a preexisting part, but this printer can print the section of the heat exchanger that is made of one material with high quality.

DED prints similarly to traditional 3D printers for plastics, where a print head moves around, adding material to the body. In DED, metal powder sprays out of the head and a laser melts the powder as the powder comes in contact with the part being printed. This process is able to blend alloys as the print progresses and is able to print on a preexisting body. Another advantage DED has over powder bed fusion is that the printing platform can sit on a five-axis table, allowing for more complicated geometries to be printed without concerns about overhangs. One drawback to DED is the lower quality of the print. DED prints are characterized by greater surface roughness and limited geometric resolution compared to powder bed fusion.

There are concerns about alloy compatibility when printing a bimetallic body or blending alloys. If the correct metals are chosen, then these concerns should be negligible. Using stainless steel for the lower temperature end and using a nickel alloy for the high-temperature end should result in good alloy compatibility, as nickel alloy and stainless steel alloy gradients have been studied before and have yielded promising results [17]. Additional research is being done here, however, since the material properties of blended alloys or bimetallic bodies are not well understood. The exact manufacturing process and the mechanical strength of the resulting bimetallic parts will be the subject of future publications.

Beyond the potential benefits of the bimetallic design of the HTR, additively manufactured heat exchangers have important design considerations that PCHEs produced with the traditional etching and diffusion bonding process do not. The high surface roughness of additively manufactured parts can significantly impact the heat transfer and friction factor in a channel [18,19], and these effects are generally not captured in 1D correlations or computational fluid dynamics (CFD) simulations. However, optimization of numerical models and comparison to experimental data show that the general trends in heat transfer and pressure loss are still present, so optimization with numerical models is still a useful approach despite the missing flow physics induced by surface roughness [20].

This study begins by briefly considering the mechanical strength of the chosen materials and a potential design. Then, 1D correlations for several candidate core designs are discussed, and a 1D heat transfer model is constructed to model the high-temperature recuperator. A multi-objective optimization is performed using the 1D model to design a bench-scale heat exchanger, and some peculiarities of the resulting designs are analyzed, focusing especially on the impact of axial conduction in this application.

2 Design of the Bi-Metal High-Temperature Recuperator

The high-temperature recuperator must operate at high temperatures and pressures, requiring high-performance materials. The low-temperature portion of the HTR is made of stainless steel 316L, and the high-temperature portion is made of Inconel 625. An intermediate module which blends these two alloys may be necessary to ensure a strong joint between the metals. This section discusses the design operating conditions of the HTR designed in this study and considers the mechanical strength of the potential core designs.

2.1 Operating Conditions and Design Constraints. Operating conditions for the HTR vary fairly significantly in other works as mass flowrate, primary heat addition, and exact cycle design change between studies. The operating conditions set for the HTR in this study do not directly reference any particular cycle, choosing instead to use temperatures and pressures similar to some seen in the literature and what seem feasible for future experimental testing on a small-scale device.

The cold fluid enters the HTR at 284 °C and 20 MPa pressure. The hot fluid enters the HTR at 500 °C and 7.8 MPa pressure. These temperatures were chosen in order to give a 200 °C temperature change in the fluids at an effectiveness of 93%. Note, however, that this goal of 93% effectiveness is for a full-scale device. A smaller device may struggle to reach this effectiveness due to limitations primarily in length.

The design resulting from the optimization in this work will eventually be manufactured for testing. As such, the device must be sufficiently compact to reduce production costs and be compatible with a small laboratory test environment. The length of the HTR core is limited to 15 cm and its total cross-sectional area should be approximately 25 cm^2, though this area is not a firm requirement and will be informed by the optimization. With the chosen temperatures and pressures, a heat duty of 300 W corresponds to a mass flowrate of approximately 1.2 g/s.

The design of the HTR is constrained by its manufacturing methods. DED is expected to be capable of producing channels as small as 1 mm^2. At this size and with a 25 cm^2 core, the flow falls solidly in the laminar flow regime. This is not consistent with full-scale heat transfer devices which generally operate with turbulent flow but is appropriate for a laboratory-scale device.

2.2 Mechanical Strength. Finite element analysis (FEA) is performed with an initial design to ensure the design concept would be suitable for the high temperatures and pressures of the HTR and determine an appropriate temperature at which to transition between materials. It is anticipated that the stress in the solid wall separating the high and low pressure fluids will be greater for the airfoil channel design than for the straight or zigzag channel designs due to the unsupported span between unit cells between the trailing edge of one airfoil and the leading edge of the next airfoil downstream. The airfoil channel design also has potential stress concentrations at the leading and trailing edges of the fins. Therefore, the airfoil channel design is expected to have reduced mechanical strength compared to the other channel shapes for comparable channel dimensions, so the strength of airfoil channel design is examined here more closely. This preliminary analysis is intended to assess the feasibility of such a unit cell design, but the mechanical strength is not the primary focus of this study. More thorough characterization of the material properties of the additively manufactured materials and the joint between stainless steel 316 and Inconel 625 are being conducted in parallel with this study and will be the topic of future works.

To accommodate the minimum feature size of DED and reduce stress concentrations at sharp corners, a 0.5 mm fillet is applied to the internal corner where the fin meets the plate, and the trailing edges of the airfoils were rounded. The part is a sectioned cut of a design with fins that are 1 mm tall, 2 mm wide, and spaced 1 mm apart, with a 2 mm stagger between adjacent fins. This FEA simulation is performed in ANSYS MECHANICAL as a static structural simulation on a unit cell of the heat exchanger core. The material properties provided by ANSYS MECHANICAL for stainless steel 316 are used for the body. Pressure loads were applied to the wetted area of the cell with 20 MPa on the top faces and 7.8 MPa on the bottom faces. Symmetric boundary conditions are applied on the planes that cut the fins into sections (top and bottom faces on the sectioned airfoils in Fig. 4). A periodic boundary condition is emulated on the front and back faces by adjoining an additional unit cell to each of these faces, then symmetric boundary conditions are applied to the front and back faces of these additional cells. The simulation uses tetragonal mesh with 167,301 elements and a basic element size of 0.2 mm. The filleted faces of the fins use a refined tetragonal mesh with a basic element size of 0.085 mm to ensure a sufficient number of elements across the curved surface.

As shown in Fig. 4, the maximum stress in the part is 113 MPa and is located in the middle of the trailing edge of the fin. This stress appears to be due primarily to the tension and compression forces in the space between consecutive airfoils.

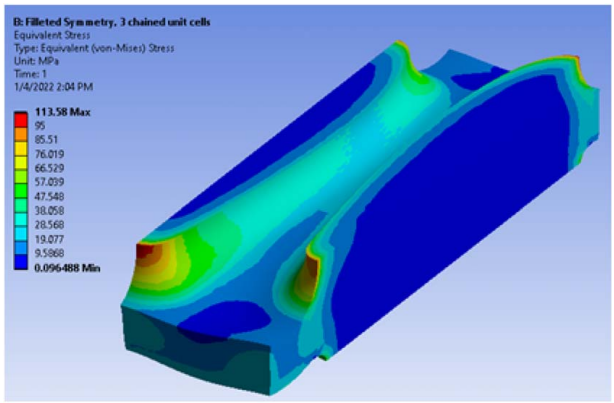

Fig. 4 Finite element analysis of an airfoil fin channel

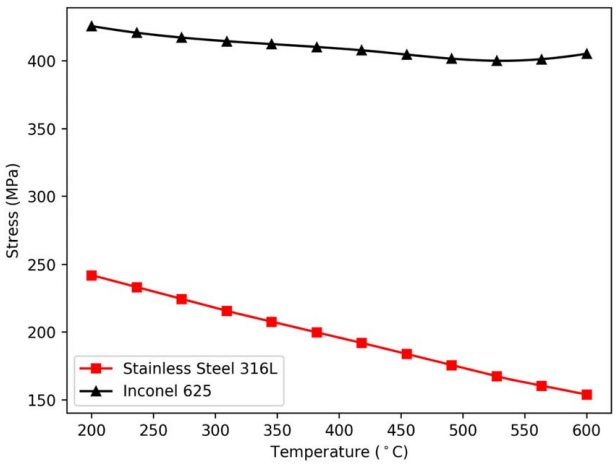

Fig. 5 Yield strength (0.2% offset) for stainless steel 316L and Inconel 625

Stainless steel 316L is to be used in the low-temperature portion of the HTR and Inconel 625 in the high-temperature portion. Yield strength for each material is plotted as a function of temperature in Fig. 5 [21,22]. The yield strength of SS316L decreases by 20% from 300 °C to 500 °C, and at 500 °C the yield strength is approximately 1.5 times the maximum stress observed in the finite element analysis. A transition temperature of 400 °C is selected, providing a safety factor of approximately 1.7.

3 Recuperator Model

The high-temperature recuperator is modeled as a counterflow heat exchanger using 1D heat transfer and friction factor models. This section outlines the operating conditions for which the HTR is designed, explains the parameterization of the unit cell design, and constructs a 1D model for the HTR with variable fluid and solid properties.

3.1 One-Dimensional Correlations. The HTR is modeled after existing PCHE designs in order to take advantage of heat transfer and friction factor correlations in the PCHE literature. We consider three channel designs: straight channels, zigzag channels, and airfoil fin channels.

Fluid flow in straight channels is a classical problem that has been studied extensively with analytic solutions for laminar flow. For turbulent flow, the Colebrook equation is used to determine the friction factor, and the Dittus–Boelter correlation is used to calculate the Nusselt number [23,24].

More recently, zigzag channels have been proposed as a way to increase heat transfer performance at the expense of greater pressure drop. Kim and No [25] developed correlations for laminar flow in zigzag channels with a 15 deg angle, while using channels with a 45 deg angle for turbulent flow.

Airfoil fin channels were proposed as a way to maintain heat transfer performance while significantly reducing pressure drop. Yoon et al. [26] developed correlations for PCHEs with National Advisory Committee for Aeronautics (NACA) 0020 airfoil fins, then compared the performance of these various channel types based on overall heat transfer coefficient in various flow conditions. They found that the airfoil fin channels had similar overall heat transfer coefficients to the zigzag channels in turbulent flow and significantly higher heat transfer coefficients in laminar flow. One-dimensional Nusselt number and friction factor correlations for each of these channel designs are summarized in Table 1.

Of the correlations listed in Table 1, only the friction factor correlation for turbulent flow in a straight channel (the Colebrook equation) accounts for surface roughness. Additive manufacturing processes tend to produce extremely rough surfaces compared to other manufacturing techniques, and this surface roughness can increase friction and heat transfer. While some work has been done to quantify the impact of the surface roughness characteristic of AM processes (e.g., Refs. [18,19]), there is no scaling method applicable to all 1D heat transfer and friction factor correlations. As such, the effect of surface roughness is not accounted for in this study. However, greater surface roughness should increase f and Nu for all channel types, so the effect may be of less concern when considering designs of different channel shapes with the 1D models than when comparing the 1D correlations to experimental data.

These correlations are plotted in Fig. 6. The zigzag channels have the greatest Nusselt number but at the cost of friction factor being much greater as well. The airfoil fin channels have a lower friction factor than the other channel types, with this difference being very pronounced for $\mathrm{Re} > 2300$. This very low friction factor for similar Reynolds number makes the airfoil fin channels of interest for further study because minimizing pressure loss can be key to overall cycle efficiency and economical operation, given that a sufficient level of heat transfer performance is still achieved.

The airfoil design also has the property of having "communicating" channels, meaning that flow may move from one channel to

Table 1 Nusselt number and friction factor correlations for various channel types

Channel shape	Laminar	Turbulent
Straight [23,24]	$f \cdot \mathrm{Re} = 15.78$ $\mathrm{Nu} = 4.089$	$\frac{1}{\sqrt{f}} = -2\log\left(\frac{e/D_h}{3.7} + \frac{2.51}{\mathrm{Re}\sqrt{f}}\right)$ $\mathrm{Nu} = 0.023\mathrm{Re}^{0.8}\mathrm{Pr}^{n}$
Zigzag [25]	$f \cdot \mathrm{Re} = 15.78 + 0.004868\mathrm{Re}^{0.8416}$ $\mathrm{Nu} = 4.089 + 0.00365\mathrm{RePr}^{0.58}$	$f = 0.1942\mathrm{Re}^{-0.091}$ $\mathrm{Nu} = 0.1696\mathrm{Re}^{0.629}\mathrm{Pr}^{0.317}$
Airfoil [26]	$f \cdot \mathrm{Re} = 9.31 + 0.028\mathrm{Re}^{0.86}$ $\mathrm{Nu} = 3.7 + 0.0013\mathrm{Re}^{1.12}\mathrm{Pr}^{0.38}$	$f \cdot \mathrm{Re} = 9.31 + 0.028\mathrm{Re}^{0.86}$ $\mathrm{Nu} = 0.027\mathrm{Re}^{0.78}\mathrm{Pr}^{0.4}$

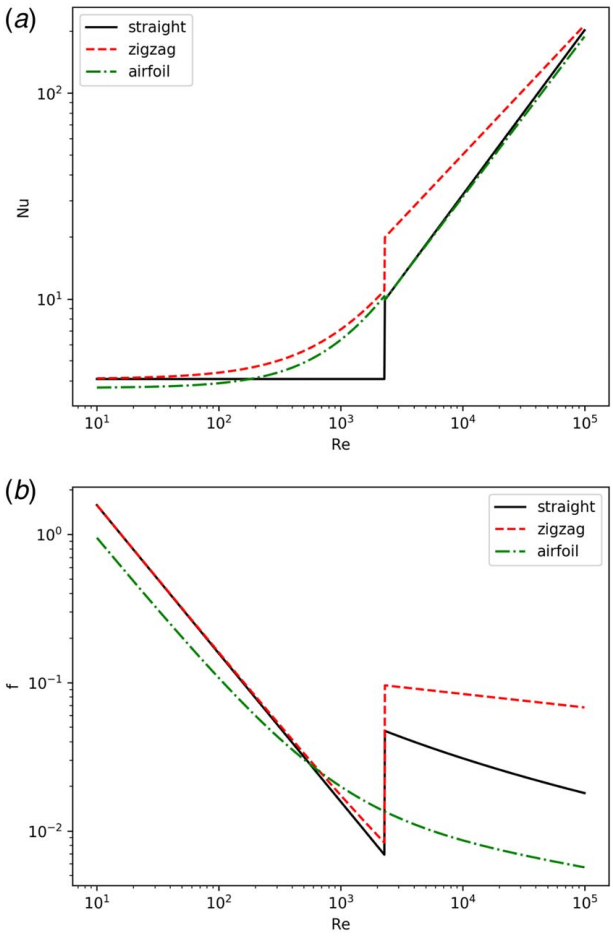

Fig. 6 Correlations for (*a*) Nusselt number and (*b*) friction factor for straight, zigzag, and airfoil fin channels

another. This can help to achieve uniform flow distribution and improve thermal-hydraulic performance [27]. The straight and zigzag designs both lack this helpful characteristic.

3.2 Unit Cell Design Parameterization. To model the HTR, the HTR core is divided into unit cells, each containing one hot fluid channel, one cold fluid channel, and one half of the wall thickness between channels around the outside of the unit cell. This is visualized in Fig. 7. The design of the HTR core is parameterized by the width of the channels w, with the channel widths being required to be equal, the height of the hot and cold channels l_H and l_C, respectively, the wall thickness between the hot and cold fluids t_p, the wall or fin thickness between channels of the same pressure t_w, and the number of unit cells N. The labeled control volume is used when constructing the 1D heat exchanger model. There are $2N$ control volumes in the heat exchanger core. The straight channels and zigzag channels both have constant cross sections defined by this parameterization. The channel size parameters for the airfoil fin channels define the minimum distance between airfoil faces. In other words, the centerline-to-centerline spacing of the fins is equal to $w + t_w$. For all of these channel types, the Reynolds number used in the correlations in Table 1 is

$$\mathrm{Re} = \frac{4\dot{m}_{\mathrm{chan}}}{\pi D_h \mu} = \frac{4\dot{m}_{\mathrm{tot}}}{N\pi\mu w l/(w+l)} \tag{1}$$

3.3 One-Dimensional Counterflow Heat Exchanger Model. Taking the heat transfer and friction factor correlations of Table 1, a 1D model of a counterflow heat exchanger can be

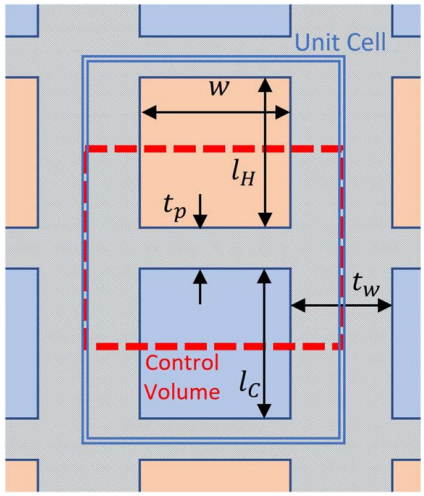

Fig. 7 Unit cell and control volume with shape parameterization

developed to model the HTR. From the definition of the Nusselt number, the heat transfer coefficient is

$$h = \frac{\mathrm{Nuk}}{D_h} \tag{2}$$

where k is the thermal conductivity of the fluid, and D_h is the hydraulic diameter of the channel.

From here, the convective thermal resistances can be calculated. This is done following the method used in [28], which uses the overall surface efficiency, η_0, such that

$$R'_{\mathrm{conv}} = \frac{1}{\eta_0 hp} \tag{3}$$

where p is the wetted perimeter of the channel. The conductive thermal resistance then only needs to account for the conduction directly across length t_p. This leaves

$$R'_{\mathrm{cond}} = \frac{t_p}{k_w w} \tag{4}$$

where k_w is the thermal conductivity of the wall material.

The thermal conductivity of the wall is allowed to vary by temperature and material by interpolating tabular values for each material to give two functions for conductivity, $k_{w,\mathrm{ss}}(T)$ for SS316 and $k_{w,\mathrm{inc}}(T)$ for In625 [21,22]. Then, some transition temperature is used to define when each materials' function is used, so that

$$k_w(T) = \begin{cases} k_{w,\mathrm{ss}}(T), & T < T_{\mathrm{trans}} \\ k_{w,\mathrm{inc}}(t), & T \geq T_{\mathrm{trans}} \end{cases} \tag{5}$$

A transition temperature of 400 °C is used in accordance with the stress analysis performed earlier.

Finally, these results can be collected into a total thermal resistance:

$$R'_{\mathrm{tot}} = R'_{\mathrm{conv},H} + R'_{\mathrm{cond}} + R'_{\mathrm{conv},C} \tag{6}$$

This quantity is then used to determine the heat transfer rate between the channels. Neglecting axial conduction, this is equivalent to the energy lost or gained by the fluid in each channel across a control volume, so this is denoted as

$$\frac{\mathrm{d}\dot{q}}{\mathrm{d}x} = \frac{T_H(x) - T_C(x)}{R'_{\mathrm{tot}}} \tag{7}$$

This can then be used to express the rate of change in the enthalpy of each fluid:

$$\frac{di_H}{dx} = \frac{d\dot{q}/dx}{\dot{m}}$$
$$\frac{di_C}{dx} = \frac{d\dot{q}/dx}{\dot{m}} \tag{8}$$

Note that the signs of both of these rates of change are the same. This is due to the counterflow configuration of the recuperator.

Similarly, the pressure drop rate can be calculated from the Fanning friction factor f, so

$$\frac{dP}{dx} = -2f\frac{\rho}{D_h}\left(\frac{\dot{m}/N}{\rho w l}\right) = -\frac{2f\dot{m}}{D_h N w l} \tag{9}$$

where the l used is either l_h or l_c, depending on which channel is being examined. For pressure drop, this sign convection holds when integrating in the direction of flow.

Taking Eqs. (8) and (9) together, we form a system of differential equations which fully describe the state of both fluids at any point along the recuperator. This system is

$$\begin{cases} \dfrac{di_C}{dx} = \dfrac{d\dot{q}/dx}{\dot{m}} \\ \dfrac{di_H}{dx} = \dfrac{d\dot{q}/dx}{\dot{m}} \\ \dfrac{dP_C}{dx} = -\dfrac{2f_C\dot{m}_C}{D_{h,C}Nwl_c} \\ \dfrac{dP_H}{dx} = \dfrac{2f_H\dot{m}_H}{D_{h,H}Nwl_h} \end{cases} \tag{10}$$

where the x direction moves from low-temperature side of the recuperator (at the cold channel inlet and hot channel outlet) to the hot side of the recuperator. This system of equations in Eq. (10) define a boundary value problem with Dirichlet boundary conditions

$$\begin{cases} i_C(x=0) = i_{C,0} \\ i_H(x=L) = i_{H,L} \\ P_C(x=0) = P_{C,0} \\ P_H(x=L) = P_{H,L} \end{cases} \tag{11}$$

The ordinary differential equation method defined by Eqs. (10) and (11) is used instead of the effectiveness-number of transfer units (ε-NTU) method in order to model variation in fluid properties, which can vary significantly when near the critical point of the fluid.

This boundary value problem can be solved by restructuring the problem as an initial value problem. This is done by assuming an outlet condition on one side of the heat exchanger (e.g., the hot channel state at $x=0$), then iteratively refining this outlet condition until the solution at $x=L$ is sufficiently close to the value defined by the boundary values there. This is known as a shooting method.

Specifically, this has been implemented as solving the initial value problem with the RK45 method. Then, the guess of the outlet condition is updated by trying to minimize the root mean square (RMS) error

$$\text{RMS} = \sqrt{\left(\frac{i_{H,\text{IVP}} - i_{H,0}}{i_{H,0}}\right)^2 + \left(\frac{P_{H,\text{IVP}} - P_{H,0}}{P_{H,0}}\right)^2} \tag{12}$$

where 0 subscript indicates the true inlet values and IVP subscript indicates the value resulting from solving the initial value problem. This minimization problem is then solved numerically.

Axial conduction through the solid was neglected in this derivation. However, some previous works (e.g., Ref. [29]) have noted that axial conduction can reduce the effectiveness of PCHEs in some applications. The effect of axial conduction can be estimated with the axial conduction parameter

$$\lambda = \frac{1}{R_{\text{ac}}\dot{C}_{\min}} \tag{13}$$

where $R_{\text{ac}} = L/k_w\ A_w$ and $\dot{C}_{\min} = \min(\dot{m}_H c_{p,H}, \dot{m}_C c_{p,C})$. The wall area A_w used in this calculation depends on the channel shape being used. For the straight and zigzag channels,

$$A_{w,\text{straight}} = A_{w,\text{zigzag}} = N\left[2wt_p + t_w\left(l_C + l_H + 2t_p\right)\right] \tag{14}$$

This includes all of the solid area for a given cross section. For the airfoil fin channels, the fins do not run the full length of the heat exchanger. They provide a thermal break, limiting conduction, so this area is not included for this shape. Therefore,

$$A_{w,\text{airfoil}} = 2Nwt_p \tag{15}$$

Axial conduction can be neglected for very small values of λ. For small but not negligible values of λ, approximately $0.01 \le \lambda \le 0.1$, loss in heat transfer performance can be approximated as

$$\varepsilon_{\text{ac}} \approx \varepsilon_{\text{nac}} - \lambda \tag{16}$$

where

$$\varepsilon_{\text{nac}} = \frac{\dot{C}_H\left(T_{H,\text{in}} - T_{H,\text{out}}\right)}{\dot{C}_{\min}\left(T_{H,\text{in}} - T_{C,\text{in}}\right)} \tag{17}$$

Rather than include axial conduction terms in the governing system of equations in Eq. (10), which would significantly increase the computational complexity of the model, this low-λ approximation for effectiveness is used when evaluating the performance of a potential design.

In the interest of reducing λ for fixed inlet fluid states and mass flowrates, and equivalently a constant $\dot{C}_{\min}$, care must be taken to choose a design which has a large R_{ac}. Without increasing L or using a material with a lower k_w, this can only be accomplished by selecting a design with small A_w. This could mean using fewer unit cells in the HTR core or choosing a channel design with thermal breaks in the heat exchanger walls, like those accomplished by using fins instead of continuous walls.

3.4 Optimization Methodology. The most desirable design of the recuperator is one which will simultaneously maximize heat transfer and fluid dynamic performance while meeting size and mechanical strength requirements and minimizing building, operation, and maintenance costs of the component. This design problem is often simplified to one or two key metrics to make it more tractable, with effectiveness and pressure drop being common optimization objectives (see Refs. [30–32]). However, the bench-scale HTR considered in this study is expected to operate at very low mass flowrates in order to achieve high effectiveness and large temperature changes in a small device, so pressure drop is expected to be negligible. Therefore, an optimization for effectiveness and device size would be more appropriate in this application.

Previous studies have provided cost estimates for PCHEs manufactured with etching and diffusion bonding in terms of \$/kg or \$/m^3 for the device (e.g., Refs. [16,33]). It is difficult to determine an appropriate unit price for the bimetallic modular HTR design due to the novelty of the manufacturing process, but the device size is an essentially exact substitute for this cost for constant cost per volume.

The optimization problem for the HTR design is then formulated to be

$$\begin{aligned} &\text{Minimize } f(w, l_C, l_H, N) = [-\varepsilon_{\text{ac}}, A_c] \\ &\text{subject to } 1\,\text{mm} \le w \le 3\,\text{mm} \\ &\qquad 1\,\text{mm} \le l_C \le 5\,\text{mm} \\ &\qquad 1\,\text{mm} \le l_H \le 5\,\text{mm} \\ &\qquad N \ge 30 \\ &\qquad A_c \le 36\,\text{cm}^2 \end{aligned} \tag{18}$$

Here, A_c is the total cross-sectional area of the recuperator core and is calculated as $A_c = N\ (l_c + l_h + 2\ t_p)(w + t_w)$. The specified constraints were determined based on mechanical strength and manufacturability constraints. The minimum channel dimensions are dictated by the minimum wall thicknesses capable with current DED manufacturing capabilities, the maximum width w is limited by the mechanical strength of the material, and the maximum channel heights l_c and l_h and minimum number of unit cells N are chosen to ensure the assumptions of symmetry and periodicity made in the 1D model held. The remaining geometric parameters are fixed, with $L = 15$ cm, $t_p = 1$ mm, and $t_w = 2$ mm, and the inlet fluid states are as described in Sec. 2.1. The multi-objective optimization is performed with the elitist non-dominated sorting genetic algorithm (NSGA-II) [34].

The result of such a multi-objective optimization is one or more solutions which all satisfy some optimal balance of the objective functions. These solutions are called non-dominated solutions because for each optimal solution, there does not exist another solution which has both a superior value in some objective while being at least equal in all of the other objectives. In other words, one objective cannot be improved without the degrading of another. This family of non-dominated solutions forms a manifold called the Pareto front. Some other metric or heuristic—manufacturing concerns, cost, and size to name a few—can then be used to choose one of these Pareto-optimal solutions.

4 Results

The multi-objective optimization was successful at finding a family of optimal solutions. As expected, the maximum achievable effectiveness increases as the overall cross-sectional area of the heat exchanger core increases. In other words, increasing heat transfer area increases the amount of heat transferred relative to a fixed maximum amount of heat transfer. The maximum effectiveness observed in the optimization is 88.4%. This is seen in the Pareto front visualized in Fig. 8.

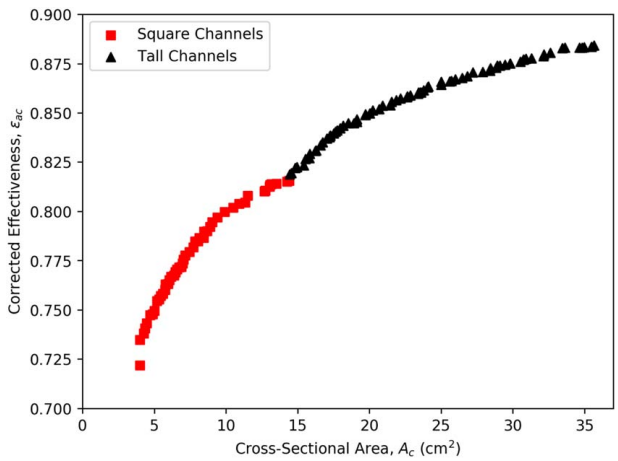

Fig. 8 Pareto front of corrected effectiveness ε_{ac} and cross-sectional area A_c

Table 2 Designs present among the Pareto-optimal solutions

Parameter	Square channel design	Tall channel design
w	1.0	1.0
l_c	1.0	8.5
l_h	1.0	9.5

There are two main designs which appear in the Pareto front (summarized in Table 2). For cross-sectional areas below 14.5 cm^2, designs with small, square channels are preferred. For all of the designs below that point, each channel has $w \approx l_h \approx l_c \approx$ 1 mm with varying values of N. The exact values of the channel size parameters vary slightly to better match the given A_c. These square channel designs achieve a maximum corrected effectiveness of 81.6%. This design falls at the bottom of the allowable ranges for the parameters.

Above that threshold, all of the designs still have a width w of about 1 mm but have cold channel heights of around 8.5 mm and hot channel heights around 9.5 mm. This design achieves a maximum effectiveness of 88.4% with the maximum allowed cross-sectional area of 36 cm^2. The small square channel design appears to be favored at the lower cross-sectional areas only because the larger channel design does not meet the constraint of $N \ge 30$ at these lower values of A_c. Since that constraint on N is only heuristic and is in place in the interest of maintaining the validity of the unit cell assumption made when developing the 1D model, it can be concluded that the design with the larger channels is superior to the smaller channel design, given that the boundary condition assumptions of the unit cell are approximately true, regardless of the number of unit cells in the heat exchanger core.

Interestingly, the effectiveness advantage of the taller channels is not due to enhanced heat transfer, but to a reduction in axial conduction. It can be shown that the ratio of axial conduction parameters $\lambda_{sq}/\lambda_{\text{tall}}$ is equal to the ratio of the number of unit cells N_{sq}/N_{tall}, which is constant across all values of A_c (ignoring rounding) since the cross-sectional area of each unit cell design is constant. For the two designs at hand, $\lambda_{sq}/\lambda_{\text{tall}} = 5$. However, it has been noted in previous studies that high aspect ratio channels may have superior heat transfer performance for microchannel heat exchangers [35], so it can be anticipated that these results may hold for cases with negligible axial conduction, as well.

Since λ for each design will increase with increasing A_c, this also implies that the effect of axial conduction will become increasingly pronounced as the total cross-sectional area grows. Figure 9 shows how the corrected and uncorrected effectiveness of each design

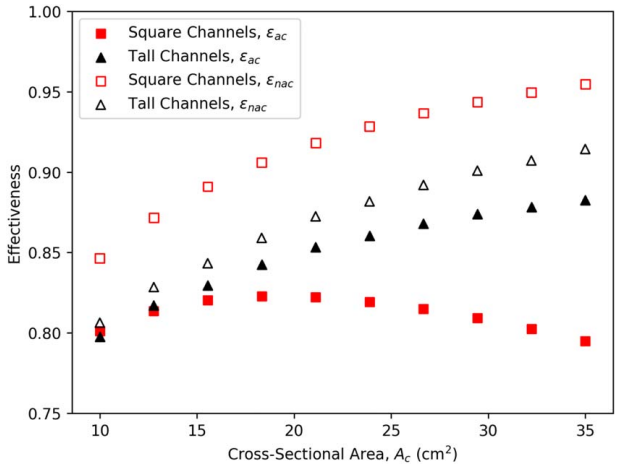

Fig. 9 Effect of axial conduction on effectiveness at various cross-sectional areas

varies with A_c (or equivalently, with the inverse of $\dot{m}$ in each channel). The difference between the ε_{nac} and ε_{ac} values is exactly equal to λ. For the square channel design, λ becomes so great around $A_c = 18\ \text{cm}^2$ that it more than negates any benefit from increasing heat transfer area. The tall channel design, however, is not penalized nearly as much for axial conduction and increased area corresponds to increased effectiveness across the whole range of A_c considered here.

It is because of the performance penalty of axial conduction that neither of these designs is able to achieve the desired $\varepsilon \geq 93\%$. Again, larger-scale versions of this device are expected to experience much less axial conduction. This is due to increases in L and $\dot{m}/N$ which both contribute to reducing λ.

Reducing pressure drop is also of interest. Though pressure drop was not included in the multi-objective optimization due to both designs operating at very low Reynolds numbers (200–600), and thus with rather negligible pressure drop, it can still be valuable to compare the pressure drop between the designs. Heat transfer devices almost always operate solidly in the turbulent regime—Reynolds numbers between 30,000 and 50,000 are typical—but a design with lower pressure drop in laminar flow should also have a lower pressure drop regardless of Reynolds number, though the actual difference at other values of Re may be unclear.

Figure 10 shows the pressure in each fluid along the length of the HTR for both designs. The tall channels have less than one tenth of the pressure drop of the square channels, experiencing a drop of 0.65 Pa and 0.31 Pa in the hot and cold fluids, respectively. This is a final reason to favor the tall channel design over the square channel design. As the HTR design is scaled up, mass flowrate per channel can be increased substantially, bringing both increased heat transfer per unit area and increased pressure loss.

The 1D HTR model also calculates the mean fluid temperatures along the length of the heat exchanger but are not corrected for axial conduction. The 1D model was compared to initial CFD results (the focus of pending work) for model validation, but the 1D model and CFD results differed fairly significantly near the inlet and outlet areas of the HTR. In fact, it was this discrepancy which prompted the examination of the impact of axial conduction on these designs. Approximate outlet temperatures can be calculated from the corrected effectiveness. Temperature profiles of the two designs are shown in Fig. 11. As shown earlier, the square channel outperforms the tall channel design when axial conduction is not considered. This is reflected in the greater temperature change in each fluid shown in Fig. 11.

In summary of these results, the tall channel design appears to be superior to the square channel design. The tall channel design experiences both reduced pressure loss and reduced heat transfer performance loss due to axial conduction. The tall channel design has less solid volume than the square channel design, and this may result in being cheaper to manufacture and make removing excess powder from the powder bed fusion process easier, reducing post-processing time. Therefore, we will analyze only the tall channel design in the accompanying sensitivity analysis.

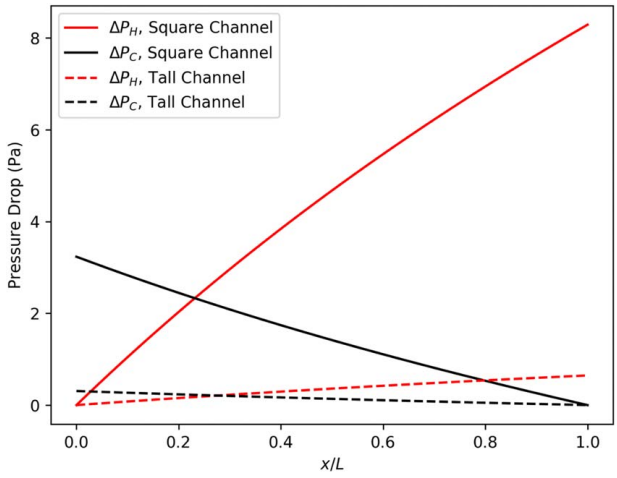

Fig. 10 Pressure drop in each fluid in both HTR designs

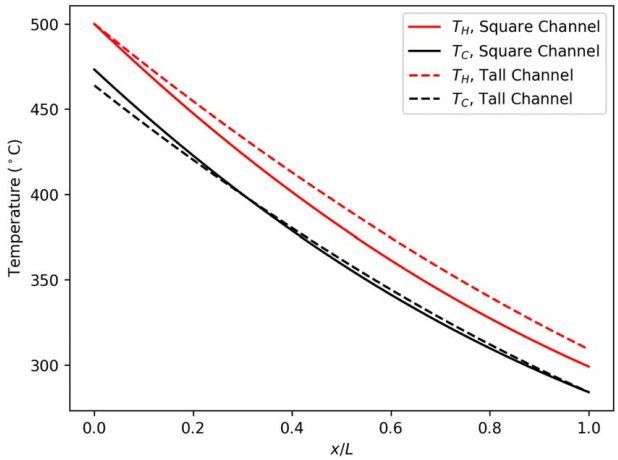

Fig. 11 Temperature profiles, neglecting axial conduction effects

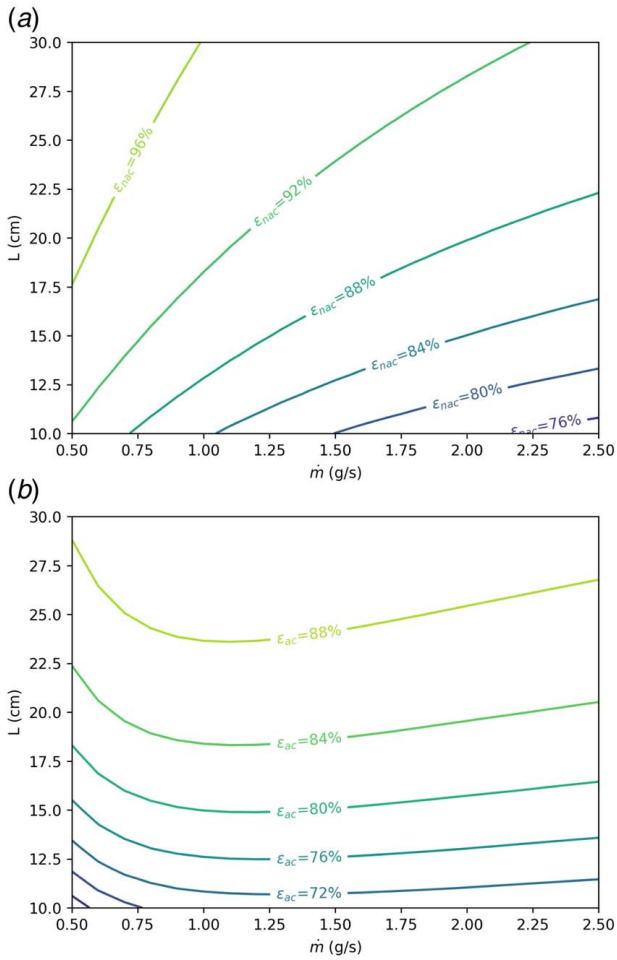

Fig. 12 Sensitivity of effectiveness with and without axial conduction to mass flowrate and core length for the tall channel design: (*a*) no axial conduction and (*b*) with axial conduction

4.1 Sensitivity Analysis. Significant axial conduction has a marked effect on the sensitivity of effectiveness to changes in various design parameters. Of principle interest is the effect of mass flowrate and heat exchanger length on effectiveness since these two parameters play a large role in determining λ and thus the corrected effectiveness ε_{ac}.

Figure 12 shows the effect of varying mass flowrate $\dot{m}$ and core length L on effectiveness, showing contours of ε. Qualitatively, effectiveness becomes much less sensitive to mass flowrate when considering axial conduction. Figure 12(*b*) also shows the interesting phenomenon of effectiveness actually increasing as mass flowrate is increased for a given value of L at low mass flowrates. This opposite usual intuition of greater mass flowrates decreases the temperature change of the fluids.

The design point of $\dot{m} = 1.2$ g/s and $L = 15$ cm lies very near the local minimum of contours of effectiveness. In other words, the design has been optimized to suit the operation conditions well. However, the curvature of the contours also means that any variation in mass flowrate—an increase or a decrease—will result in a loss of effectiveness while also minimizing sensitivity to variation in mass flowrate. This behavior is not seen when neglecting axial conduction, where the response surface is monotonic. This change in sensitivity to mass flowrate near the minima of the effectiveness contours warrants further investigation either experimentally or with CFD.

5 Conclusions

Closed Brayton cycles using sCO_2 as a working fluid are likely candidates for future high-temperature applications due to their potential cost benefits. Reducing the total cost of the turbomachinery and heat transfer equipment in such a power cycle is fundamental to realizing these cost benefits in practice. One potential method for doing this for the high-temperature recuperator used in many sCO_2 Brayton cycles is the bi-metal HTR discussed in this work. In this work, an initial design for such an HTR is explored, considering straight, zigzag, and airfoil fin channel designs seen in PCHEs. Airfoil fin designs appear to be most favorable given that they can achieve comparable heat transfer performance to zigzag channels without the downside of such significant pressure loss.

A 1D model is developed for the HTR, modeling the HTR core as a counterflow heat exchanger. This model allows for variable fluid properties. Two candidate designs for airfoil fin HTRs are determined through multi-objective optimization. In the process of comparing these designs, it is seen that axial conduction plays a significant role in differentiating the performance of these designs, with the design with a greater number of small channels being more heavily impacted by axial conduction as the mass flowrate in each unit cell decreased. The design with larger channels was more robust to variation in mass flowrate since it reduced the effect of axial conduction on effectiveness by minimizing the amount of continuous material running the length of the HTR through which heat can conduct. As the design of the HTR is shifted to larger scales and higher per-channel mass flowrates, axial conduction will not play as large of a role in the effectiveness of the device.

A small-scale HTR will be manufactured in the near future to validate the bi-metal design and manufacturing approach of the proposed HTR with hydrostatic pressure testing.

There is ongoing work parallel to this design work to characterize the mechanical strength of the metals deposited by powder bed fusion and DED and the interface of the two materials. As more data are collected on the material properties of the metals being used, they will be incorporated into the design and analysis processes. Also, CFD simulation is being used to validate the results of this 1D optimization and explore channel design variations and modifications not captured by the 1D correlations used here. This is the subject of a forthcoming work.

Additive manufacturing offers much more design freedom than more traditional manufacturing methods. Future iterations of the HTR may move away from PCHE-based designs towards designs which play to the strengths of additive manufacturing: complex geometries which truly maximize performance and that are impossible to produce with other techniques. Future gains in heat transfer performance, pressure loss reduction, and construction cost minimization may all contribute to further reducing the cost of energy from sCO_2 Brayton cycles.

Conflict of Interest

There are no conflicts of interest.

Data Availability Statement

The datasets generated and supporting the findings of this article are obtainable from the corresponding author upon reasonable request.

Nomenclature

e = surface roughness
f = Fanning friction factor
h = heat transfer coefficient
i = specific enthalpy
k = thermal conductivity
l = channel height
$\dot{m}$ = mass flowrate
p = wetted perimeter
$\dot{q}$ = heat transfer rate
t = thickness
w = channel width
x = axial location
L = heat exchanger core length
N = number of unit cells in the heat exchanger core
P = absolute pressure
R' = thermal resistance per unit length
T = temperature
c_p = specific heat capacity
A_c = total cross-sectional area of the heat exchanger core
$\dot{C}_{\min}$ = minimum fluid capacitance rate
D_h = hydraulic diameter
Nu = Nusselt number
Pr = Prandtl number
Re = Reynolds number

Greek Symbols

ε = heat exchanger effectiveness
η_0 = overall surface efficiency
λ = axial conduction parameter
μ = dynamic viscosity
ρ = fluid density

Subscripts

ac = axial conduction
airfoil = airfoil fin channel type
chan = channel
cond = conductive
conv = convective
C = cold channel
H = hot channel
inc = Inconel 625
IVP = initial value problem
L = at $x = L$
nac = no axial conduction
p = "plate" between hot and cold fluids
ss = stainless steel 316
straight = straight channel type

tot = total
trans = transition between metals
w = wall or fin between channels of the same fluid
zigzag = zigzag channel type
0 = at $x = 0$

Abbreviations

sCO_2 = supercritical carbon dioxide
CFD = computational fluid dynamics
CSP = concentrating solar power
DED = directed energy deposition
FEA = finite element analysis
HTR = high-temperature recuperator
PCHE = printed circuit heat exchanger
PBF = powder bed fusion
RMS = root mean square
STHE = shell and tube heat exchanger

References

[1] You, D., and Metghalchi, H., 2021, "On the Supercritical Carbon Dioxide Recompression Cycle," ASME J. Energy Resour. Technol., **143**(12), p. 121701.
[2] He, Y.-L., Qiu, Y., Wang, K., Yuan, F., Wang, W.-Q., Li, M.-J., and Guo, J.-Q., 2020, "Perspective of Concentrating Solar Power," Energy, **198**, pp. 1–11.
[3] Turchi, C., Ma, Z., Neises, T., and Wagner, M., 2013, "Thermodynamic Study of Advanced Supercritical Carbon Dioxide Power Cycles for Concentrating Solar Power Systems," ASME J. Sol. Energy Eng., **135**(4), p. 041007.
[4] "Quadrennial Technology Review 2015: Advancing Clean Electric Power Technologies—Supercritical Carbon Dioxide Brayton Cycle," 2015, Tech. Rep., U.S. Department of Energy.
[5] Kwon, J. S., Son, S., Heo, J. Y., and Lee, J. I., 2020, "Compact Heat Exchangers for Supercritical CO_2 Power Cycle Application," Energy Convers. Manage., **209**(Apr.), p. 112666.
[6] Noaman, M., Awad, O., Morosuk, T., Tsatsaronis, G., and Salomo, S., 2022, "Identifying the Market Scenarios for Supercritical CO_2 Power Cycles," ASME J. Energy Resour. Technol., **144**(5), p. 050906.
[7] Carlson, M., and Alvarez, F., 2021, "Design of a 1 MWth Supercritical Carbon Dioxide Primary Heat Exchanger Test System," ASME J. Energy Resour. Technol., **143**(9), p. 090904.
[8] Black, J., Straub, D., Robey, E., Yip, J., Ramesh, S., Roy, A., and Searle, M., 2020, "Measurement of Convective Heat Transfer Coefficients With Supercritical CO_2 Using the Wilson-Plot Technique," ASME J. Energy Resour. Technol., **142**(7), p. 070901.
[9] Deshmukh, A., Kapat, J., and Khadse, A., 2021, "Transient Thermodynamic Modeling of Air Cooler in Supercritical CO_2 Brayton Cycle for Solar Molten Salt Application," ASME J. Energy Resour. Technol., **143**(2), p. 022013.
[10] Nikitin, K., Kato, Y., and Ngo, L., 2006, "Printed Circuit Heat Exchanger Thermal–Hydraulic Performance in Supercritical CO_2 Experimental Loop," Int. J. Refrig., **29**(5), pp. 807–814.
[11] Chai, L., and Tassou, S. A., 2020, "A Review of Printed Circuit Heat Exchangers for Helium and Supercritical CO_2 Brayton Cycles," Therm. Sci. Eng. Prog., **18**, p. 100543.
[12] Liu, G., Huang, Y., Wang, J., and Liu, R., 2020, "A Review on the Thermal-Hydraulic Performance and Optimization of Printed Circuit Heat Exchangers for Supercritical CO_2 in Advanced Nuclear Power Systems," Renew. Sustain. Energy Rev., **133**, p. 110290.
[13] Faizan, M., and Almerbati, A., 2023, "Evolutionary Design of Compact Counterflow Heat Exchanger," ASME J. Energy Resour. Technol., **145**(3), p. 032102.
[14] Mekki, B. S., Langer, J., and Lynch, S., 2021, "Genetic Algorithm Based Topology Optimization of Heat Exchanger Fins Used in Aerospace Applications," Int. J. Heat Mass Transfer, **170**, p. 121002.
[15] Høghøj, L. C., Nørhave, D. R., Alexandersen, J., Sigmund, O., and Andreasen, C. S., 2020, "Topology Optimization of Two Fluid Heat Exchangers," Int. J. Heat Mass Transfer, **163**, p. 120543.
[16] Kwon, J. G., Kim, T. H., Park, H. S., Cha, J. E., and Kim, M. H., 2016, "Optimization of Airfoil-Type PCHE for the Recuperator of Small Scale Brayton Cycle by Cost-Based Objective Function," Nucl. Eng. Des., **298**, pp. 192–200.
[17] Carroll, B. E., Otis, R. A., Borgonia, J. P., Suh, J.-O., Dillon, R. P., Shapiro, A. A., Hofmann, D. C., Liu, Z. -K., and Beese, A. M., 2016, "Functionally Graded Material of 304L Stainless Steel and Inconel 625 Fabricated by Directed Energy Deposition: Characterization and Thermodynamic Modeling," Acta Mater., **108**, pp. 46–54.
[18] Stimpson, C. K., Snyder, J. C., Thole, K. A., and Mongillo, D., 2016, "Roughness Effects on Flow and Heat Transfer for Additively Manufactured Channels," ASME J. Turbomach., **138**(5), p. 051008.
[19] Stimpson, C. K., Snyder, J. C., Thole, K. A., and Mongillo, D., 2017, "Scaling Roughness Effects on Pressure Loss and Heat Transfer of Additively Manufactured Channels," ASME J. Turbomach., **139**(2), p. 021003.
[20] Kirsch, K. L., and Thole, K. A., 2018, "Isolating the Effects of Surface Roughness Versus Wall Shape in Numerically Optimized, Additively Manufactured Micro Cooling Channels," Exp. Therm. Fluid Sci., **98**, pp. 227–238.
[21] AK Steel, 2016, 316/316L Stainless Steel Product Data Bulletin, https://asremavad.com/wp-content/uploads/2018/11/AK-steel-316-stainless-steel-data-sheet.pdf.
[22] Special Metals, 2013, INCONEL alloy 625, https://www.specialmetals.com/documents/technical-bulletins/inconel/inconel-alloy-625.pdf.
[23] Colebrook, C. F., 1939, "Turbulent Flow in Pipes, With Particular Reference to the Transition Region Between the Smooth and Rough Pipe Laws," J. Inst. Civil Eng., **11**(4), pp. 133–156.
[24] Dittus, F., and Boelter, L., 1985, "Heat Transfer in Automobile Radiators of the Tubular Type," Int. Commun. Heat Mass Transfer, **12**(1), pp. 3–22.
[25] Kim, I. H., and No, H. C., 2011, "Thermal Hydraulic Performance Analysis of a Printed Circuit Heat Exchanger Using a Helium–Water Test Loop and Numerical Simulations," Appl. Therm. Eng., **31**(17), pp. 4064–4073.
[26] Yoon, S. H., No, H. C., and Kang, G. B., 2014, "Assessment of Straight, Zigzag, S-Shape, and Airfoil PCHEs for Intermediate Heat Exchangers of HTGRs and SFRs," Nucl. Eng. Des., **270**, pp. 334–343.
[27] Kirsch, K. L., and Thole, K. A., 2018, "Numerical Optimization, Characterization, and Experimental Investigation of Additively Manufactured Communicating Microchannels," ASME J. Turbomach., **140**(11), p. 111003.
[28] da Silva, R. P. P., Mortean, M. V. V., de Paiva, K. V., Beckedorff, L. E., Oliveira, J. L. G., Brandão, F. G., Monteiro, A. S., Carvalho, C. S., Oliveira, H. R., Borges, D. G., and Chastinet, V. L., 2021, "Thermal and Hydrodynamic Analysis of a Compact Heat Exchanger Produced by Additive Manufacturing," Appl. Therm. Eng., **193**, p. 116973.
[29] Baek, S., Kim, J.-H., Jeong, S., and Jung, J., 2012, "Development of Highly Effective Cryogenic Printed Circuit Heat Exchanger (PCHE) With Low Axial Conduction," Cryogenics, **52**(7), pp. 366–374.
[30] Li, Y. Z., Xie, Y. H., and Zhang, D., 2019, "Optimization Investigation on Wavy Channel Printed Circuit Heat Exchanger for Solar Energy Powered Brayton Cycle," IOP Conf. Ser.: Mater. Sci. Eng., **556**(1), p. 012038.
[31] Yang, Y., Li, H., Yao, M., Zhang, Y., Zhang, C., Zhang, L., and Wu, S., 2020, "Optimizing the Size of a Printed Circuit Heat Exchanger by Multi-objective Genetic Algorithm," Appl. Therm. Eng., **167**, p. 114811.
[32] Wang, W., Li, B., Tan, Y., Li, B., and Shuai, Y., 2022, "Multi-objective Optimal Design of NACA Airfoil Fin PCHE Recuperator for Micro-gas Turbine Systems," Appl. Therm. Eng., **204**, p. 117864.
[33] Gezelius, K., 2004, "Design for Compact Intermediate Heat Exchangers for Gas Cooled Fast Reactors," Master's thesis, Massachusetts Institute of Technology, Boston, MA.
[34] Deb, K., Pratap, A., Agarwal, S., and Meyarivan, T., 2002, "A Fast and Elitist Multiobjective Genetic Algorithm: NSGA-II," IEEE Trans. Evol. Comput., **6**(2), pp. 182–197.
[35] Collins, I. L., Weibel, J. A., Pan, L., and Garimella, S. V., 2019, "Evaluation of Additively Manufactured Microchannel Heat Sinks," IEEE Trans. Components Packag. Manuf. Technol., **9**(3), pp. 446–457.